Nanoscale

Understanding the Role of AgNO3 Concentration and Seed Morphology to Achieve Tunable Shape Control in Gold Nanostars

Journal:	*Nanoscale*
Manuscript ID	NR-ART-09-2018-007615.R1
Article Type:	Paper
Date Submitted by the Author:	07-Jan-2019
Complete List of Authors:	Atta, Supriya; Rutgers University, Chemistry and Chemical Biology Beetz, Michael; Ludwig-Maximilians-Universitat Munchen Fabris, Laura; Rutgers University, Materials Science and Engineering

Journal Name

ARTICLE

Understanding the Role of $AgNO_3$ Concentration and Seed Morphology to Achieve Tunable Shape Control in Gold Nanostars

Supriya Atta,[a] Michael Beetz,[b] and Laura Fabris[c*]

Received 00th January 20xx,
Accepted 00th January 20xx

DOI: 10.1039/x0xx00000x

www.rsc.org/

Gold nanostars are one of the most fascinating anisotropic nanoparticle. The morphology of a nanostar can be controlled by changing various synthetic parameters; however, the detailed growth mechanism is still not fully understood. Herein, we investigate this process in six-branched nanostars, focusing first on the properties of the single crystalline seed, which evolves to include penta-twinned defects as the gateway to anisotropic growth into the 6-branched morphology. In particular, we report on a high-yield seed-mediated protocol for the synthesis of these particles with high dimensional monodispersity in the presence of Triton-X, ascorbic acid, and $AgNO_3$. Detailed spectroscopic and microscopic analyses have allowed the identification of several key intermediates in the growth process, revealing that it proceeds via penta-twinned intermediate seeds. Importantly, we report the first experimental evidence tracking the location of silver with sub-nanometer resolution and prove its role as a stabilizing agent in these highly branched nanostructures. Our results indicate that metallic silver on the spikes stabilizes the nanostar morphology and that the remaining silver, present when $AgNO_3$ is added at high concentration, deposits on the core and between the bases of neighboring spikes. Importantly, we also demonstrate the possibility to achieve dimensional monodispersity, reproducibility, and tunability in colloidal gold nanostars that are substantially higher than previously reported, which could be leveraged to carry out holistic computational-experimental studies to understand, predict, and tailor their plasmonic response.

Introduction

Among the various types of gold nanoparticle systems providing features facilitating field localization, gold nanostars have been widely recognized owing to their tunable plasmon resonances, which have the potential to be extended from the visible to the infrared.[1-4] Generally speaking, there is a strong correlation between optical properties and morphology in plasmonic nanoparticles, with sharp edges and tips being further able to create localized electric field enhancement in proximity to the nanoparticle's surface. Due to the structure- and size-dependence of the localized surface plasmon resonance (LSPR) bands, morphological control during the synthesis is very important.[5-6] For instance, we have observed how small differences in the shape and number of branches of a nanostar lead to drastic shifts in the LSPR band position and width, with highly branched nanostars being characterized by broad and blue shifted resonances.[7] For this reason, an increasing number of synthetic procedures have been developed to control the size and shape of plasmonic nanoparticles, among which both seeded and non-seed mediated methods have shown to afford morphological tunability.[8-10] Importantly, it is crucial to obtain colloidal nanoparticles with high yield and reproducibility and large batch monodispersity. However, while good tunability in the synthesis of anisotropic nanoparticles has been achieved in the case of short, low aspect ratio branches,[11] morphological control in gold nanostars with high aspect ratio features is still not satisfactory.[3, 12-13] To improve dimensional monodispersity and reproducibility in gold nanostars (i.e. the ability to consistently obtain nanostars with exactly the same length both within and among batches), it is necessary to develop a fundamental understanding of the role of the chemical variables and their impact on the growth mechanism, and to investigate the key factors affecting growth. One of the issues in achieving this goal (particularly in highly branched nanostructures) has been so far the difficulty to trap reaction intermediates due to the generally fast reaction kinetics for these particles, and to understand, as a consequence, how any ill-defined morphology can affect the final products.[14] One of the goals of this work was therefore to develop a fundamental understanding of the growth mechanism of gold nanostars characterized by few spikes with high shape anisotropy and to identify a simple synthetic methodology that could yield highly monodispersed gold nanostars with consistent reproducibility. Importantly, while some progress has been made in the mechanistic understanding of the growth of branched nanostructures[15-16] still much needs to (and should) be understood for branched nanostructures with high aspect ratio features, especially for their promising role in optics and plasmonics.

The use of Ag^+ is common in seed-mediated syntheses of gold nanostars to tune the spike morphology up to a certain length by gradually increasing $AgNO_3$ concentration in the growth solution.[17] This phenomenon is similar to what observed in gold

[a] Department of Chemistry and Chemical Biology, Rutgers University, Piscataway NJ, 08854 USA
[b] Department of Chemistry and Center for NanoScience (CeNS), Ludwig Maximilians Universität München, 81377 Munich, Germany.
[c] Department of Materials Science and Engineering, Rutgers University, Piscataway NJ, 08854 USA

nanorods.[18-20] However, while several mechanisms have been proposed to explain in detail the role of $AgNO_3$, they are still highly debated despite the decade-long scientific efforts.[19] For example, a face-specific cetyltrimethylammonium-Br-Ag^+ capping complex was hypothesized to be formed to block specific gold facets thus leading to the formation of nanorods.[21] In another proposed mechanism, underpotential deposition (UPD) of monolayers or sub-monolayers of silver on the gold nanorod surface was invoked as the factor leading to anisotropic growth.[22] In this mechanism, silver deposits on the surface of the nanorods and selectively blocks selected facets, such as the {110}, rather than others, for instance {100} or {111}.[23] Unfortunately, while the presence of trace amounts of silver has been reported on the surface of the gold nanorods,[23-25] a mechanistic investigation on the role of $AgNO_3$ at different concentrations in the growth of gold nanorods or nanostars has not been carried out yet. In this respect, structural and elemental characterization could provide essential insight into the growth mechanism, ultimately allowing to improve the monodispersity and reproducibility of gold nanostars.

In this manuscript, we describe a novel type of gold nanostar, that we define as 6-branched based on the dominating number of spikes obtained from the statistical analysis of several particles imaged at various tilt angles with scanning transmission electron microscopy (STEM) and reported in Figure S1 (panel m). For these particles, we elucidate the role of the synthetic parameters employed in the surfactant-based seed-mediated protocol followed to synthesize them. We also propose a growth mechanism that focuses on the properties of the seeds and how they affect the final nanoparticle morphology. These nanoparticles show exceptionally high dimensional monodispersity compared to nanostar systems reported before,[26-29] and can be synthesized with high tunability and reproducibility. The reduced number of spikes, whose length and shape can be rationally controlled, limits side-by-side spike cross-talk, thus reducing LSPR peak broadening, and enables establishing fundamental relationships between morphology and plasmonic properties, which has been not possible so far due to the irreproducibility of the traditional synthetic protocols for gold nanostars.[30] For these reasons, these nanoparticles represent the first example of branched nanostructure that can be synthesized by design to possess pre-determined physical and optical properties. Based on this potential, it is important to understand the role of the reagents and their interplay during nanostar growth. To address this need, we performed a systematic study to determine how the concentrations of the surfactant (Triton X), the reducing agent (ascorbic acid), and $AgNO_3$, and their interaction with the evolving seeds affect the morphology, and thus the LSPR bands, of the resulting gold nanostars. By investigating the mechanism of gold nanostar formation in this surfactant-mediated synthesis, we propose a kinetically-controlled process as the basis of the growth.

Results and discussion

We define this novel type of gold nanostar as 6-branched because the majority of the produced nanoparticles has six branches, even though a closer look reveals a non-zero number of particles with spike number between 3 and 7. To confirm that the statistical distribution obtained via traditional 2D TEM micrographs correctly portrays the tridimensionality of the nanostructure, we carried out tomographic reconstruction of a ca. 70 nm-spike sample, and observed that indeed the number of discernible spikes varied with the tilt angle in the tomogram (Figure 1). For instance, the number of spikes of a typical star at 0, 40, and 230 degrees is five, six, and four, respectively (Figure S1a, S1b, and S1d). To overcome this issue, we determined as the maximum number of spikes for a nanostar the maximum number measured after exploring all possible orientations in the multiparticle tilt series reported in Figures S1 g-l. The statistical analysis shows that the product is a mixture of branched nanoparticles with three to seven spikes with ~1% spherical impurities, even in the absence of purification. To determine the average spike length for these nanostars, we accounted for the maximum spike length of a spike taking into account the whole tilt series, and generated the statistical distribution reported in Figure S1 n). This specific sample, with average spike length of 70 nm, was obtained when the concentrations of the reagents used were 0.15 M (Triton X), 1.6 mM (ascorbic acid), 30 µM ($AgNO_3$), and 0.14 nM (seeds). Compared to the statistical distribution of spike lengths obtained with traditional dimensional analysis carried out with 2D TEM (*vide infra*), the tomographic reconstruction led to a decrease in standard deviation by a factor of ten.

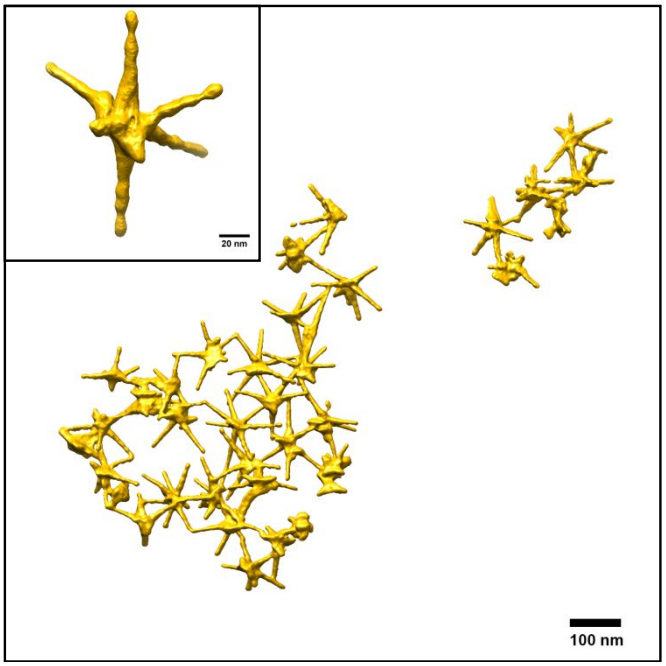

Figure 1. 3D reconstruction of a set of nanostars with 70 nm average spike length collected through STEM tomography from -60° to +60° with 10° steps. In the inset, detailed reconstruction of an individual star collected at higher magnification. From the analysis of the multi-particle sample at various tilt angles, we determined the average number of spikes, as reported in the histogram of Figure S1.

Among all the reagents needed in this synthesis, the two main recognized parameters influencing anisotropic growth are the properties of the seeds and the concentration of $AgNO_3$. However, in the specific synthesis explored in this work, investigating their interplay with the added surfactant (Triton X) and the reducing agent (ascorbic acid) also provided useful

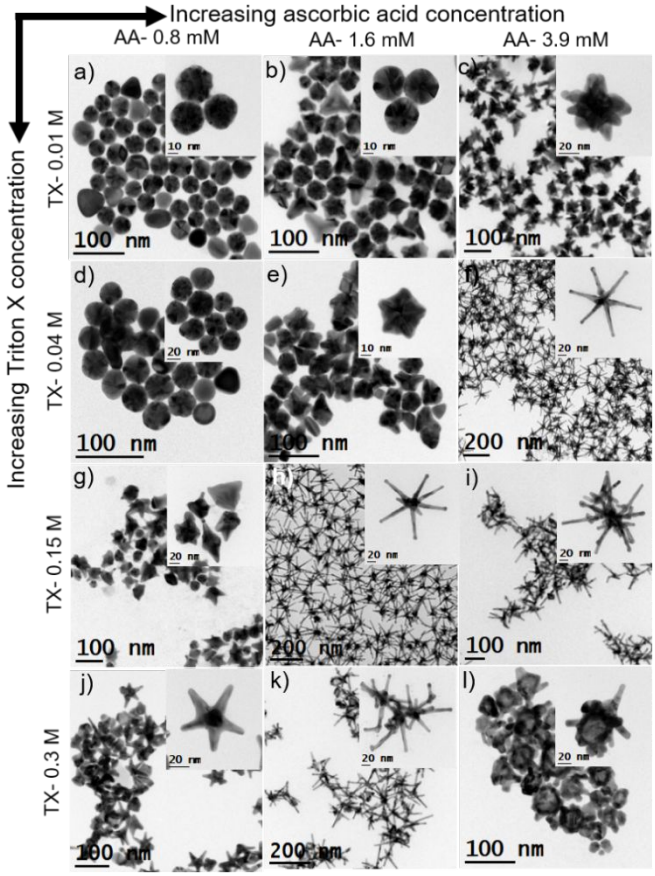

Figure 2. (a-l) TEM images of the gold nanoparticles where the concentration of the two chemical variables (Triton X and ascorbic acid) were progressively changed. In a column, the concentration of Triton X (TX) was varied from 0.01 to 0.3 M while it was kept constant in a row. For example, the concentration of Triton X in column 1 were 0.01 M (a), 0.04 M (d), 0.15 M (g), and 0.3 M (j). On the other hand, the concentration of ascorbic acid was kept constant in a column while it was increased from 0.8 mM to 3.9 mM in a row. For example, the concentration of ascorbic acid in row 1 were 0.8 mM (a), 1.6 mM (b), and 3.9 mM (c). The concentrations of $AgNO_3$ (100 µM) and seeds (0.14 nM) were kept constant.

insight. Nonetheless, our primary goal was to first understand how seed evolution and silver concentration and position affect the growth and yield high shape anisotropy in few-spiked gold nanostars. Therefore, we first carried out the synthesis varying the concentrations of the four main reagents (i.e., Triton X, ascorbic acid, $AgNO_3$, and seeds) and characterized the obtained nanoparticles to extrapolate trends to identify the optimal synthetic conditions to achieve 6-branched nanostars, the ideal starting point for a more in-depth analysis. In this seed-mediated synthesis, seed and growth solutions were prepared separately but with an equal concentration of surfactant, starting from concentration values similar to what reported in the initial manuscript of Pallavicini et al. but departing from them to achieve monodispersity and eliminate byproducts.[31] By varying the concentration of the four variables independently, we have investigated and determined how to obtain highly monodispersed 6-branched gold nanostars. While we are aware that multiple parameter spaces could likely provide ideal conditions to achieve similar results, we deemed it beyond the scope of this work to search for additional concentration values, considering more important to instead focus on understanding the growth mechanism in this specific set of conditions. In Figure 1, we have investigated the role of Triton X and ascorbic acid by modifying their concentrations while keeping the concentration of $AgNO_3$ and seeds constant at 100 µM and 0.14 nM, respectively. We have examined four different concentrations of Triton X (0.01 M, 0.04 M, 0.15 M, and 0.3 M), and three different concentrations of ascorbic acid (0.8 mM, 1.6 mM, and 3.9 mM). In Figure 2, the concentration of Triton X varies along a column while the concentration of ascorbic acid is kept constant. For example, in column 1 of Figure 2, the concentration of Triton X was increased from 0.01 M to 0.3 M (0.01 M (1a), 0.04 M (1d), 0.15 M (1g), and 0.3 M (1j)), while the concentration of ascorbic acid was kept constant (0.8 mM). On the other hand, the concentration of Triton X was kept constant throughout a row while the concentration of ascorbic acid was varied. For example, in row 1 of Figure 2, the concentration of ascorbic acid was increased from 0.8 mM to 3.9 mM (0.8 mM (1a), 1.6 mM (1b), and 3.9 mM (1c)) while the concentration of Triton X was kept constant (0.01 M).

TEM micrographs in Figure 2 reveal that the 6-branched morphology can be obtained only at ideal concentrations of both surfactant (Triton X) and reducing agent (ascorbic acid). In a column of Figure 2, when the concentration of Triton X was increased at a constant ascorbic acid concentration, the morphology changed from polyhedral nanoparticles to 6-branched stars. For example, in column 1 (Figure 2a, d, g, and j), the morphology of the nanoparticles changed from polyhedral to 6-branched stars at very high Triton X (0.3 M) and very low ascorbic acid (0.8 mM) concentration. However, the same change in morphology was also observed at moderately high Triton X (0.15 M) and moderate ascorbic acid (1.6 mM) concentration in column 2 (Figure 2h), and at moderately low Triton X (0.04 M) and high ascorbic acid (3.9 mM) concentration in column 3 (Figure 2f). Interestingly, at a very low concentration of Triton X (0.01M) and very high concentration of ascorbic acid (3.9 mM) (Figure 2c) multibranched stars were formed, where multiple (n>>6) branches were grown from the central core. Complex hyperbranched nanoparticles, with multiple side branches on each of the six main branches (Figure

2k, and 2i), were formed when both Triton X and ascorbic acid concentrations were higher than the ideal concentrations for 6-branched stars formation. Multibranched hollow gold nanoparticles were formed at a very high concentration of Triton X and ascorbic acid (Figure 2l); we are still investigating their mechanism of formation. We observed similar morphology changes from polyhedral to 6-branched stars to complex hyperbranched nanoparticles in a row when the ascorbic acid concentration was increased at constant Triton X concentration (Figure 2g-i).

At ideal ascorbic acid (and $AgNO_3$) concentrations for 6-branched nanostar synthesis, the final nanoparticle morphology depends strongly on the concentration of Triton X. We observed that multibranched stars were formed in the absence of Triton X (Figure S3), while hyperbranched nanostars were formed at high Triton X concentration (Figure 2k). In agreement with previous reports, it appears that at very low concentration of Triton X, gold ions are not tightly bound to the surface by the surfactant Triton X and can be easily reduced by ascorbic acid.[31] By increasing the surfactant concentration above the critical micelle concentration (CMC) of Triton X (0.3 mM), the number of Au-encapsulating Triton X micelles increases,[32] thus decreasing the amount of free Au ions. The reduction in available free Au ions leads to more controllable gold reduction and branch generation during the growth process. A similar effect has been observed in other surfactant-mediated gold nanostars syntheses, in which morphological changes from polyhedral to branched stars were also observed at increasing surfactant concentration.[29] For gold nanorods, it has been reported that a high concentration of surfactant (cetyltrimethylammonium bromide, CTAB) is necessary to

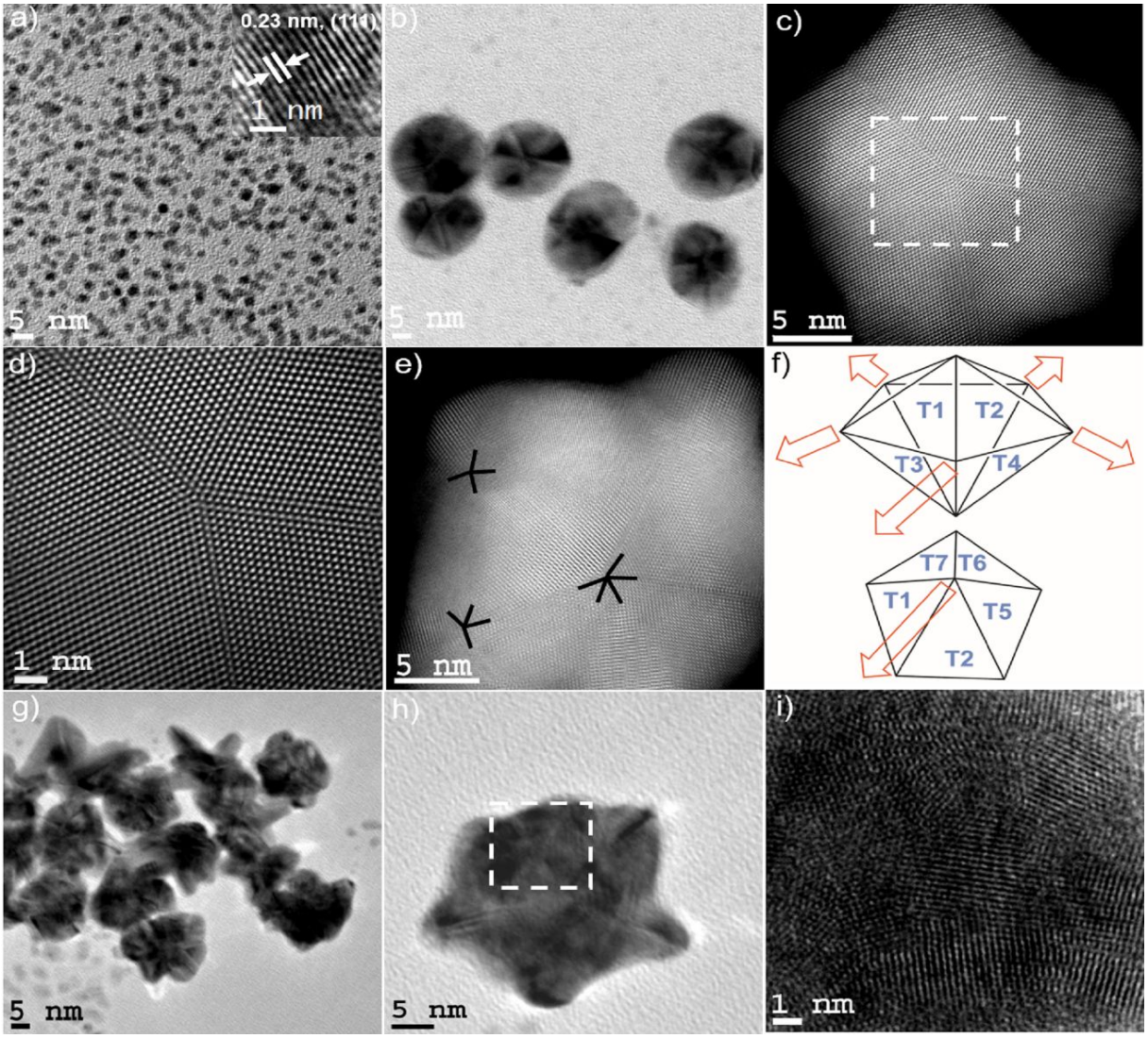

Figure 3. a) TEM micrographs of the seeds with average diameter of 3 nm. HRTEM micrograph (inset) shows the single crystalline morphology of the seed, with interplanar spacing characteristic of {111} planes in FCC gold. (b-c) TEM and STEM micrographs of penta-twinned intermediate seeds isolated within the first instants of growth of 6-branched stars. d) High resolution STEM image (FFT analysis reported in Figure S2) of the selected area of Figure 2c exhibiting a fivefold symmetry. e) STEM image of a typical penta-twinned intermediate seed showing one five-fold symmetry and two four-fold symmetry defects, which corelates to the 3D construction of decahedral morphology of penta-twinned intermediate seeds. f) Representation of spike growth from decahedral seeds. Top image: Schematic side view identifying the spike growth directions on seeds such as that reported in Figure 2e. A maximum number of five spikes can grow along the equatorial directions identified by the red arrows, which are determined by four neighbouring facets (T1, T2, T3, and T4). Bottom image: Schematic top view representing five neighbouring facets are present (T1, T2, T5, T6, and T7). g-i) TEM and HRTEM images of multiply twinned intermediate seeds isolated within the first instants of growth of multibranched stars.

achieve high aspect ratios, as high amounts of CTAB limit the number of free Au ions and reduce secondary nucleation events thus leading to the formation of longer nanorods.[33] However, because it is still unclear how micelle encapsulation for 6-branched nanostars occurs, we can only hypothesize that at extremely high concentrations of Triton X (>0.15 M) unzipping of the surfactant at the surface of the spikes may be taking place (mediated by the excess surfactant in solution) leading to the generation of secondary nucleation events on the spikes,[34] and thus resulting in the formation of hyperbranched nanostars (Figure 2k).

Ascorbic acid can tune the morphology of the resulting nanoparticles as well, with higher amounts leading to the desired 6-branched nanostars. We believe this to be due to the increase in negative charge on the growing seeds due to excess ascorbic acid in the growth solution, resulting in the migration of gold atoms toward low surface energy facets, such as {111}, from high surface energy facets like {110}, or to an increase in crystal growth kinetics at higher ascorbic acid concentration.[35-36] Clearly, additional experiments will be necessary to provide further evidence on the nature of the observed nanostar reshaping.

Having established the ideal parameter space for Triton X and ascorbic acid, we then focused our investigation on the determination of seed quality (size and crystallinity) (Figure 3a). To avoid Ostwald ripening of the seeds on the grid during TEM analysis, we employed n-pentane thiol as a capping agent to quench the reaction and stabilize the seeds, as previously done to analyze the morphology of growth intermediates. HRTEM micrographs of the seeds disclose that most of the particles have single crystalline morphology, with an interplanar spacing of 0.23 nm, typical of (111) plane in FCC gold, and diameters of around 3 nm (Figure 3a). It has been proposed that twinned seeds may be fundamental to ensure spike growth on nanostars;[17, 37] however, the direct correlation between defect nature and nanostar morphology has never been shown. We have therefore carried out a detailed analysis of the crystallographic properties of the seeds to correlate them to the resulting nanostar product. The morphology was investigated by quenching the reaction with n-pentane thiol as a capping agent 10 s after addition of Triton X, ascorbic acid, and $AgNO_3$ for 6-branched stars and multibranched stars. The morphology of the seed turned from single crystalline to twinned crystal, with all gold planes belonging to the {111} family. To be specific, penta-twinned intermediate seeds were formed when the concentration of Triton X, ascorbic acid, and $AgNO_3$ were ideal for the formation of 6-branched stars (Figure 3c), whereas multiply twinned intermediate seeds having multiple {111} facets were formed when the concentration of Triton X, ascorbic acid, and $AgNO_3$ were kept at values observed to produce multibranched stars (Figure 3g-i). Interestingly, the morphology of a typical penta-twinned intermediate seed (Figure 3e), which has one nucleation center having five different {111} facets and two nucleation centers having four different {111} facets, gives an overview of the 3D construction of the intermediate seed, which is decahedral (Figure 3f). The formation of multiple {111} facets in a multiply twinned intermediate supports our hypothesis that at high ascorbic acid concentration multiple low energy facets {111} are formed, whereas the reduction rate of gold (III) at 0.15 M Triton-X, 1.6

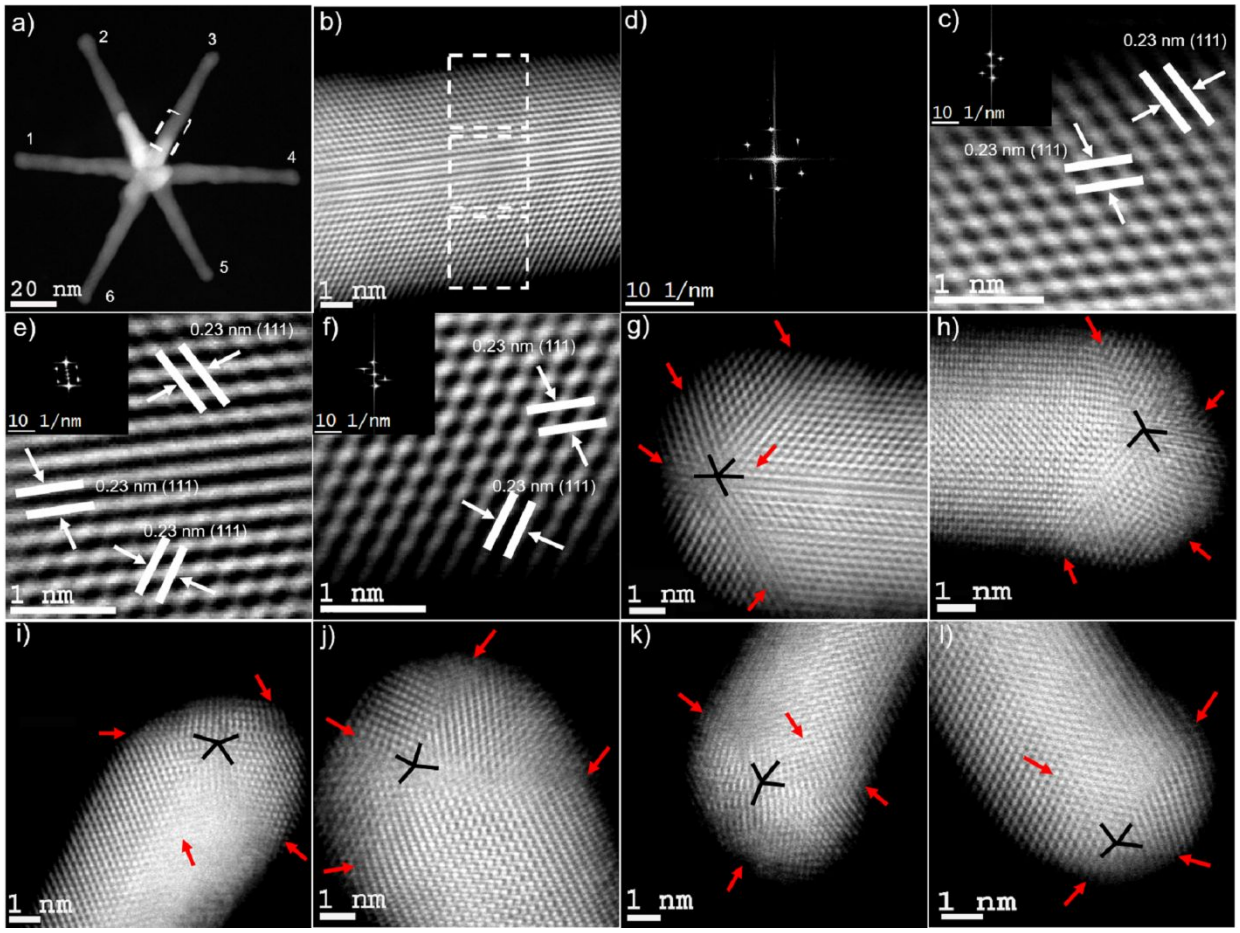

Figure 4. a) STEM image of a typical 6-branched star. (b-f) High resolution STEM images with FFT analysis on the selected area of the spike in Figure 3a showing the presence of only a twin boundary where the FFT (inset) and lattice fringes represent {111} planes reversely oriented with respect to a common twin plane. g) STEM micrograph of the tip showing five twinning planes, which indicates that the spike is forming on a twinning axis of a pentagonal unit. (h-l) STEM micrographs of the tips shows four twinning planes, indicating that the spike is forming on a twinning axis of a tetrahedral unit. Red arrows show the twin planes.

mM ascorbic acid, and 100 µM $AgNO_3$ leads only to the formation of penta-twinned defects.

Interestingly, STEM micrographs of 6-branched nanostars (Figure 4b-f) show an anisotropic growth over the {111} facets on either side of the twin boundaries for penta-twinned intermediate seeds, which arises due to low twinning energy and angle strain.[38] The corresponding fast Fourier transform image further confirms that the two {111} crystal facets are oriented with a common {111} twin plane (Figure 4e). This is further confirmed by the STEM micrographs of the tips (Figure 4g-l) which provide a clear view of the crystallographic structure of the penta-twinned seeds from which the spikes were grown, as illustrated in Figure 3f. In comparing Figure 4g-l and 3f, one can observe that while in principle these particles should possess either five or seven spikes, the distribution reported in Figure 3f identified quite comparable numbers of 5-, 6-, and 7-branched nanostars, with a higher frequency of 6-branched nanostars.

nanoparticles to 6-branched stars by increasing the concentration of $AgNO_3$ at non-ideal concentrations of Triton-X and ascorbic acid (Figure S5). We have investigated the effect of $AgNO_3$ when the concentrations of the other reagents are optimized to obtain highly monodisperse and reproducible 6-branched stars (0.15 M Triton X, 1.6 mM ascorbic acid, and 0.14 nM seeds) (Figure 2h). The concentration of $AgNO_3$ was increased in small increments of 10 µM to determine the possibility of finely-tuning the morphology through $AgNO_3$ (Figure 5 and Figure S6). The spike length increased rapidly by roughly 8 nm by increasing $AgNO_3$ concentration in 10 µM increments from 30 to 60 µM $AgNO_3$. Then it slowly increased by around 2-3 nm by increasing the amount of $AgNO_3$ from 60 to 100 µM in 10 µM steps (Figure 5k, and Figure S7 for dimensional analysis). This evolution was followed by monitoring the red-shift of the longitudinal LSPR band in the UV-Vis spectrum (Figure 5j and Figure S6). The red-shift was also accompanied by a visible change in the solution color from blue to brown as the concentration of $AgNO_3$ increased. Importantly, the narrow standard deviations in LSPR positions measured across different syntheses (Figure S6) are a clear indication of the high reproducibility afforded by our synthetic protocol. At $AgNO_3$ concentration higher than 100 µM, the spike length did not further increase (Figure 5j-k), rather a blue shift in the LSPR band, reported to indicate a shortening or thickening of the spike, was instead observed.[6, 17] The blue shift of the LSPR at 110 µM $AgNO_3$ concentration could also however be due to the deposition of atomic Ag on the core (*vide infra*), as the ascorbic

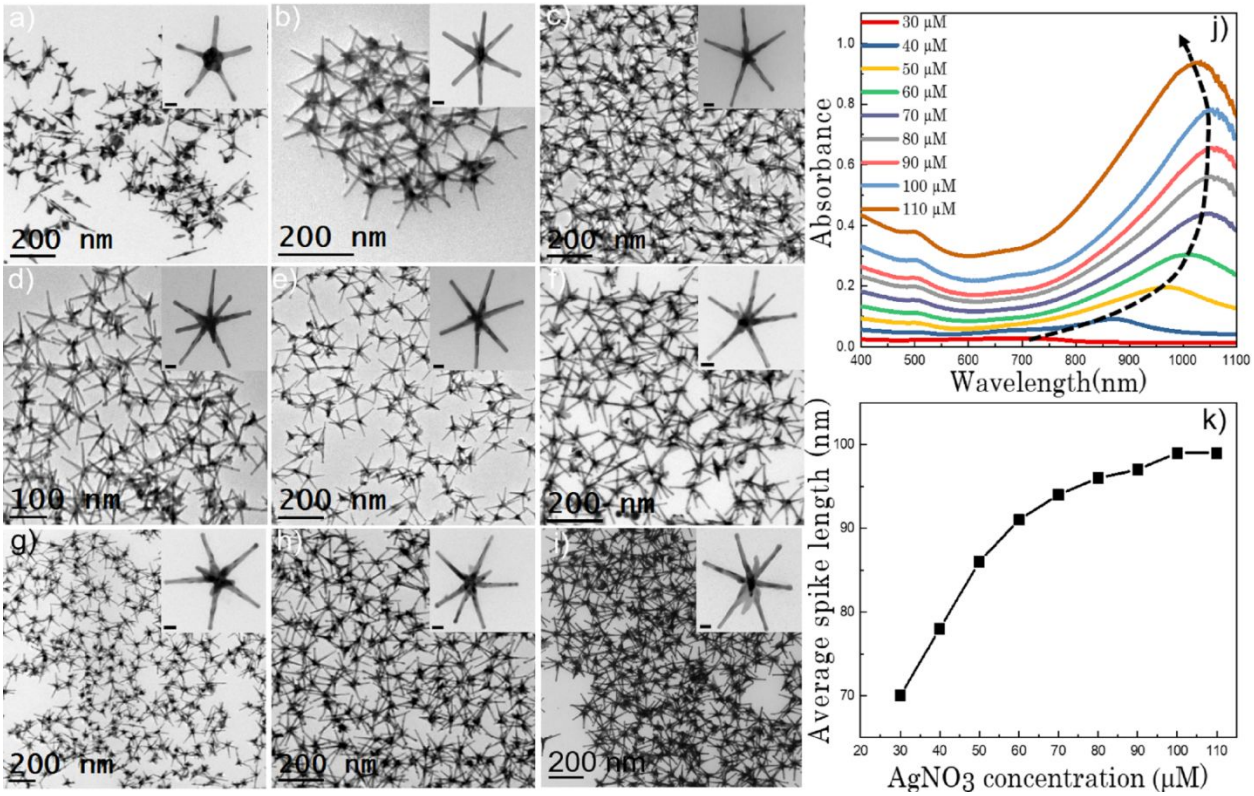

Figure 5. (a-i) TEM micrographs of nanostars formed under different $AgNO_3$ concentrations- 30 µM (a), 40 µM (b), 50 µM (c), 60 µM (d), 70 µM (e), 80 µM (f), 90 µM (g), 100 µM (h), and 110 µM (i). The concentration of other two chemical variables (ascorbic acid and Triton-X) were 1.6 mM and 0.15 M, respectively. Scale bars are 20 nm (inset). j) UV–vis spectra (normalized) for each of the colloidal dispersions which shows a gradual red shift with increasing $AgNO_3$ concentration as the spike length is increased, and blue shift after 100 µM $AgNO_3$ as silver is deposited on the core. k) Evolution of the average spike length as a function of $AgNO_3$. concentration.

We have observed that polyhedral nanoparticles were formed in the absence of $AgNO_3$, thus indicating that $AgNO_3$ is necessary for the formation of the desired 6-branched nanostars (Figure S4). $AgNO_3$ concentration affects the stability of the particle as well, as we observed spherical impurities at or below 30 µM $AgNO_3$, likely due to nanostar reshaping. However, we have not seen the transformation from polyhedral

acid in excess can reduce remaining silver ions resulting in the nanostar core diameter to increase from 25 to 35 nm. Vo-Dinh and coworkers reported that silver overgrowth on gold nanostars is possible and can blue shift the plasmon resonance of the longitudinal mode.[39]

To study the fate of silver and its role on the evolution of spike morphology, we first monitored the branch sharpness, which is the ratio between the spike widths at core and tip, observing that it increased from 1.2 to 1.9 (Figure S8) with increasing $AgNO_3$ concentration from 30 µM to 100 µM, possibly due to the migration of gold atoms from the tip toward the core. This result further motivated us to study the evolution of the spike morphology. Spike growth was investigated in detail by arresting the reaction at different time points and examining the intermediates via TEM to correlate morphology evolution to LSPR position, when the concentration of Triton X, ascorbic acid, and $AgNO_3$ were 0.15 M, 1.6 mM, and 30 µM respectively (Figure 6 and Figure S9). TEM micrographs (Figure 6a-l and Figure S9a-l) at different time intervals reveal that the branches grew gradually and reached maximum length (100 nm) after 5 minutes. After that, they shrank, and the process was completed after 12 hours, with an overall shrinking in spike length by 30 nm, from 100 nm (5 min) to 70 nm (12 hours). The time-dependent evolution of this reaction was monitored by UV-Vis spectrophotometry (Figure 6m), which elucidated that the LSPR band gradually red shifted as the spike length increased between 30 seconds and 5 minutes. The LSPR band reached its maximum redshift to 1071 nm after 5 min, then blue shifted from 1071 nm to 734 nm after 12 hours. The blue shift was associated to the migration of gold atoms from high energy

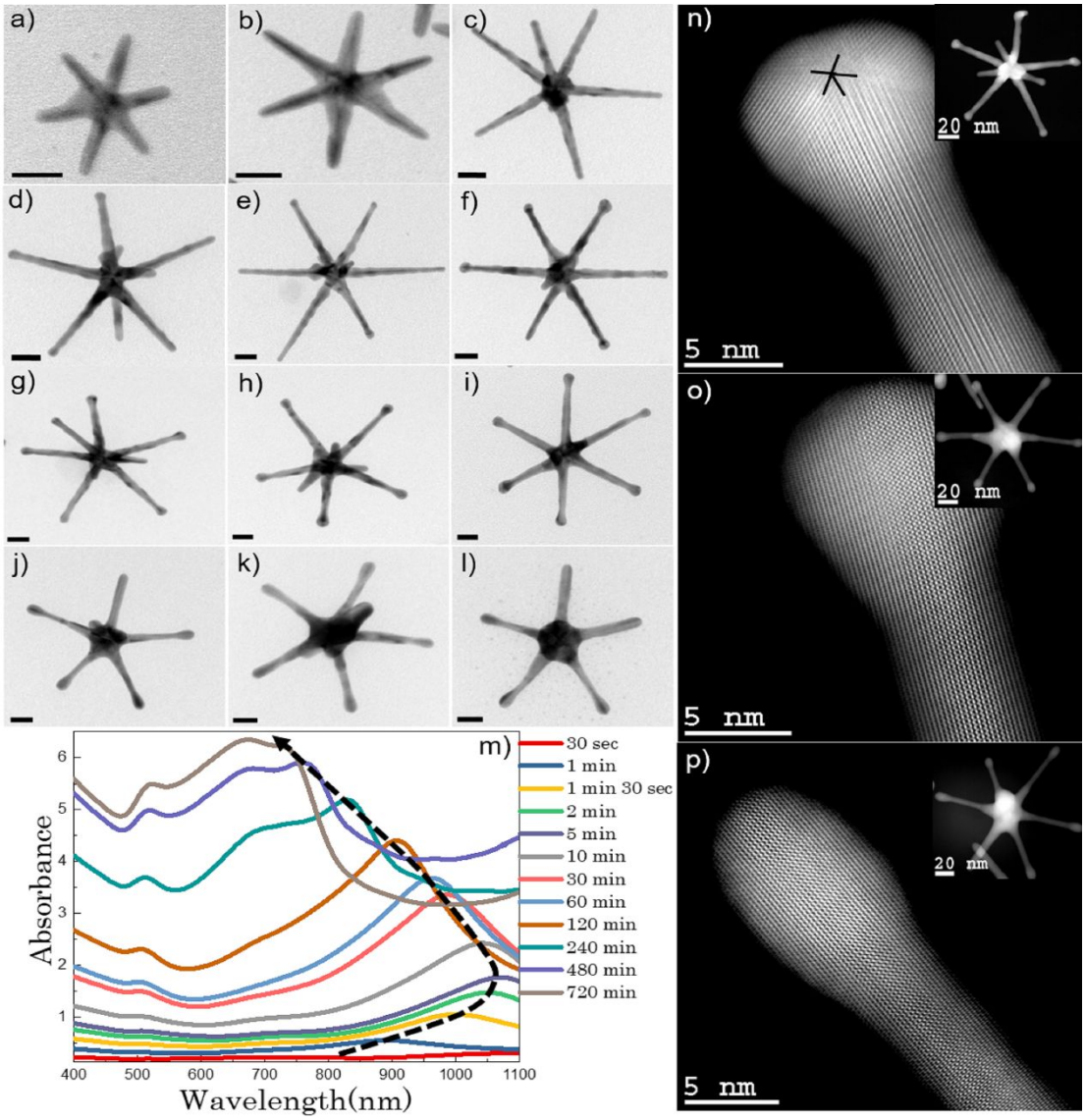

Figure 6. (a-l) TEM micrographs of gold nanostars when the concentrations of the growth solution are- Triton-X-0.15 M, ascorbic acid- 1.6 mM, and $AgNO_3$- 30 µM for which growth was arrested at the indicated reaction times (30 sec (a), 1 min (b), 1 min 30 sec (c), 2 min (d), 5 min (e), 10 min (f), 30 min (g), 60 min (h), 120 min (i), 240 min (j), 480 min (k), and 720 min (l)). m) Corresponding UV–vis spectra (normalized) taken from each aliquot sample which indicates that an initial red shift of the longitudinal plasmon peak occurred, which reversed after 5 minutes, and was followed by a permanent blue shift. Scale bars are 20 nm. (n-p) STEM micrographs of the spike at 5 min (n), 240 min (o), and 720 min (p) showing the morphology from twinned spherical tip to oblate tip.

sites on the tip toward lower energy ones at the core, resulting in a decrease in spike length from 100 nm to 70 nm. The LSPR shift was also accompanied by a visual color change in the solution from blue to green to brown to blue, as observed before for the growth of multibranched gold nanostars and gold nanorods when the spike length was reduced in the late stages of the reaction.[4, 20, 25, 40]

The nanostar morphology at 30 μM $AgNO_3$ concentration for a given growth time was further investigated by STEM (Figure 6n-p) to assess spike morphology in detail. STEM micrographs revealed that the gold nanostars grown for 5 minutes contained spherical penta-twinned tips where twin boundaries having {111} facets bridging the sides with the tips can be observed (Figure 6n). However, after 6 hours the tip was observed to be less spherical (Figure 6o) and to become oblate after 12 hours, with no clearly distinguishable facets detectable, as the penta-twinned morphology of the tips disappeared after 6 hours (Figure 6o-p). We believe that the driving force for these morphological changes is the surface energy minimization that is achieved by removing reactive edge atoms located at the twin boundaries of highly faceted penta-twinned spikes.[18, 41]

To gain further insight into the evolution of the spikes, we have investigated in detail the changes in overall nanostar morphology at the 5-minute (Figure S10) and 12-hour (Figure 5b-d, 5f, and 5h) marks, by varying the concentration of $AgNO_3$, starting from the observation that maximum spike length is reached after 5 minutes and the minimum after 12 hours, for reactions with 30 μM $AgNO_3$. We have used five different additional concentrations of $AgNO_3$ (40 μM, 50 μM, 60 μM, 80 μM, and 100 μM), and observed that the spike length is maximized after 5 minutes (100 nm) for all $AgNO_3$ concentrations, with additional substantial shape reconstruction occurring at the 12-hour time point. For nanostars synthesized with 30 μM $AgNO_3$ the shape reconstruction was substantial, with spike length reduction from 100 nm to 70 nm and loss of the sphere at the tip (Figure 6n-p). However, the extent of deformation decreased with increasing the concentration of $AgNO_3$ from 30 μM, becoming the lowest for nanostars synthesized at 100 μM $AgNO_3$ (Figure S10a-f). For instance, while a 341 nm blue shift was observed for 30 μM $AgNO_3$ stars, only a 6 nm blue shift was observed for 100 μM $AgNO_3$ stars (Figure 7a-f). We also observed visually that the color did not change from brown to blue when the concentration of $AgNO_3$ was kept at 100 μM $AgNO_3$. These results led us to postulate that the 5-minute morphology might be the kinetically trapped version of the thermodynamically-stable 12-hour morphology, and that deposited Ag atoms might reduce significantly the atom diffusion typically observed for highly energetic gold facets on gold nanoparticles. These observations also established the added important role for $AgNO_3$ (i.e., to stabilize the nanostar shape and size) beyond the well-known shape-inducing role. We attribute the shape reconstruction observed at longer reaction times for low $AgNO_3$ concentration to the fact that the highly energetic gold atoms at the tips can easily diffuse along the spike migrating to more energetically favorable positions on the nanostar, such as the base of the spike. However, when the concentration of $AgNO_3$ was 100 μM, the Ag atoms appeared to stabilize the highly energetic gold atoms, thus inhibiting their diffusion toward the core. A similar result was reported by Tong et al., who observed a blue shift of the longitudinal plasmon peak of gold nanorods when they kept from 2 hrs. to 13 weeks.[18] The possible reason behind the stability gained with a $AgNO_3$ concentration above 30 μM is the presence of a monolayer of silver atoms that stabilizes the underlying gold atoms on the surface of the nanoparticles with a Au-Ag(UPD)-Cl type of interaction.[42-43] While other interactions may be present, this appears to be the most plausible based on previous reports[23-24,42] and our

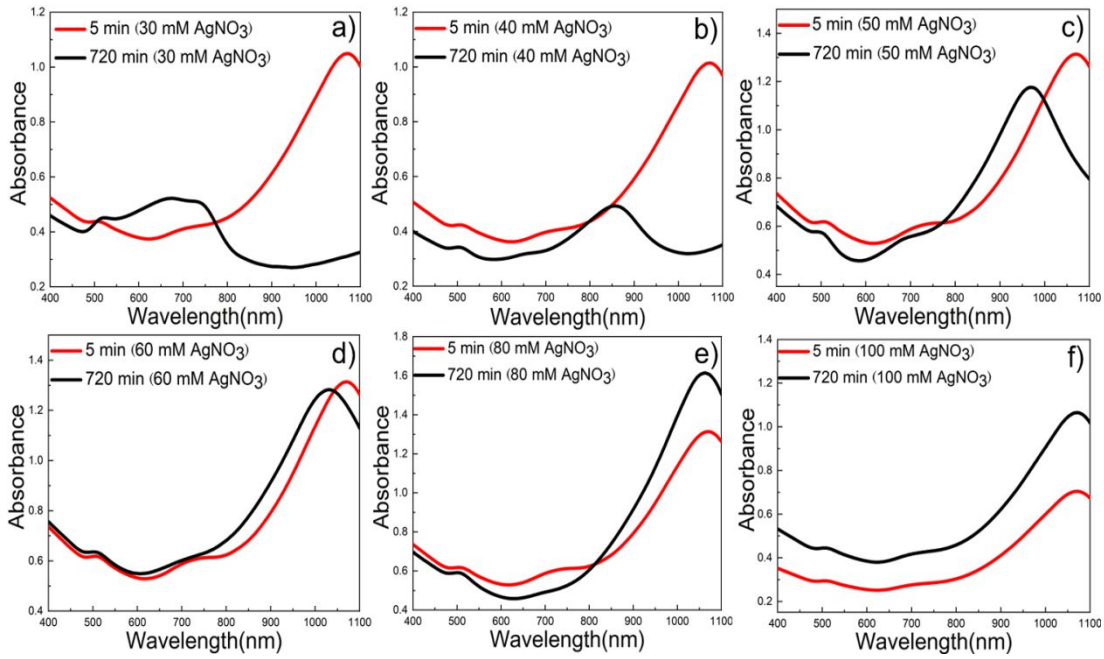

Figure 7. (a-f) UV-Vis spectra of 6-branched gold nanostars formed after 5 min and 720 min reaction time under different $AgNO_3$ concentration-30 μM (a), 40 μM (b), 50 μM (c), 60 μM (d), 80 μM (e), and 100 μM (f). UV-Vis spectrum shows a 341 nm, 212 nm, 99 nm, 42 nm, 12 nm, and 6 nm blue shift for 30 μM, 40 μM, 50 μM, 50 μM, 60 μM, 80 μM, and 100 μM $AgNO_3$ respectively.

preliminary voltammetric identification of both Ag(0) and Ag^+ in the nanostar suspension after purification (data not shown).

We have investigated further the role of Ag by using scanning transmission electron microscopy-efficiency energy dispersive X-ray spectroscopy (STEM-EDS), to determine whether or not Ag exists as adsorbed species on the Au surface or becomes fully alloyed to Au on the nanostar spike. We also wanted to

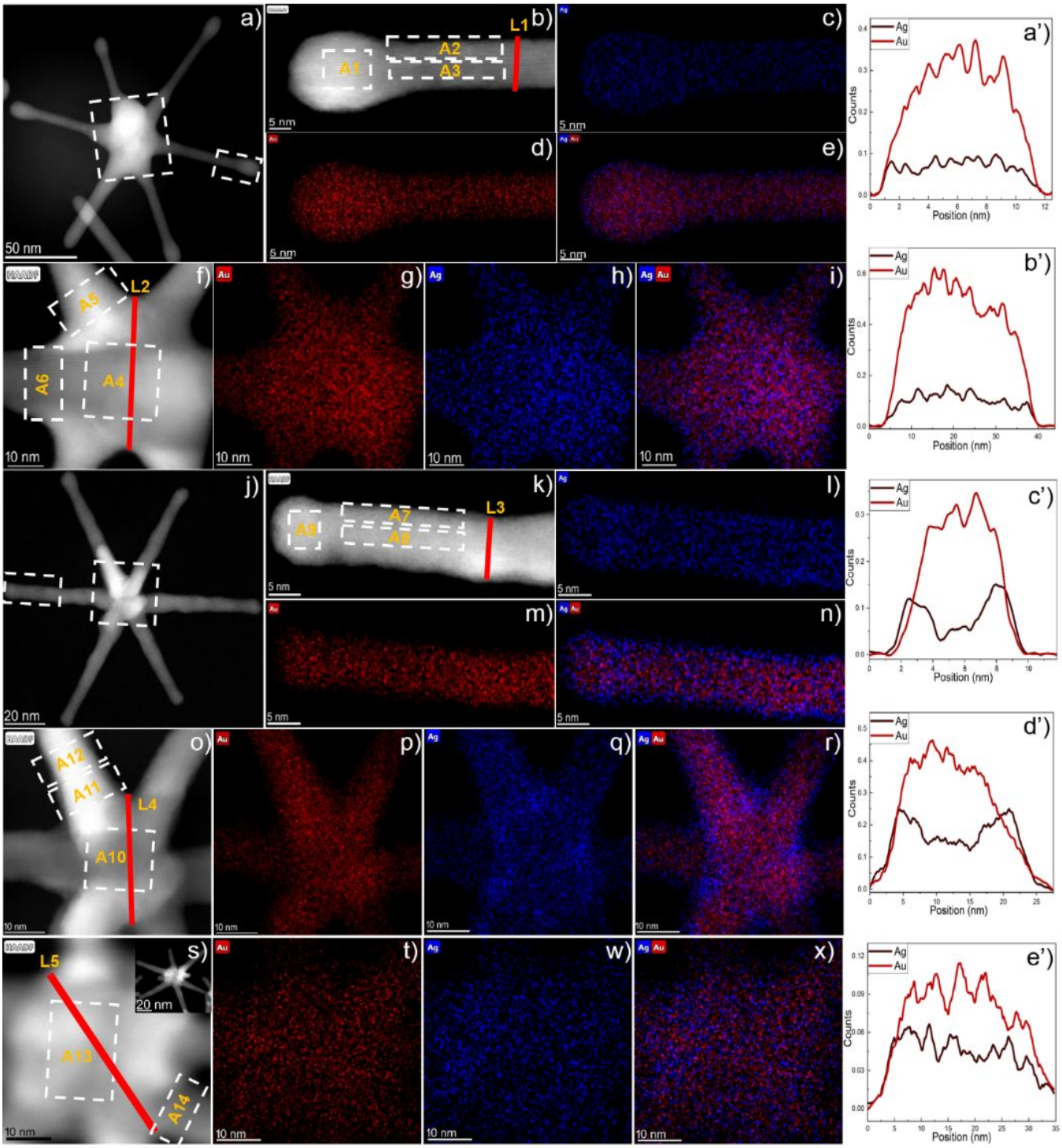

Figure 8. a) TEM micrograph and (b-i) HAADF-STEM micrograph and elemental maps of the spike (b-e) and the core (f-i) of 30 µM $AgNO_3$ after 12 hours. j) TEM micrograph and (k-r) HAADF-STEM micrograph and elemental maps of the spike (k-n) and the core (o-r) of 100 µM $AgNO_3$ after 12 hours. (s-x) HAADF-STEM micrograph and elemental maps of the core of 100 µM $AgNO_3$ after 12 hours. (a'-e') Line scan elemental profiles of 6-branched nanostars at 30 µM (spike a', and core b'), 100 µM (spike c', and core d'), and 110 µM (core e') which reveal that Au and Ag are miscible in all samples. At increasing $AgNO_3$ concentrations, metallic Ag first saturates deposition sites along the side wall of the tips, and then proceeds to deposit at the core.

ascertain whether or not the deposition of increasing amounts of silver at high concentrations of $AgNO_3$ is responsible for the observed morphology stabilization and LSPR blue shifts. Figure 8 shows the STEM image of 6-branched gold nanostars having three different $AgNO_3$ concentrations (30, 100, and 110 μM) along with corresponding STEM-EDS map showing the gold signal (red scale) and the silver signal (blue scale), which reveal that silver was alloyed with gold in the nanostars. Moreover, we have observed that the relative silver signal increased with increasing $AgNO_3$ concentration, going from 3.86% (2.21% at core, and 5.51% at spike) to 14.66% (13.87% at core, and 15.45% at spike) when the concentration of $AgNO_3$ was increased from 30 μM to 100 μM, and even further increased to 16.45% (18.94% at core, and 13.97% at spike) when the concentration of $AgNO_3$ was 110 μM. Interestingly, the line-scanned EDS elemental profiles of the spike and the core of 30 μM $AgNO_3$ showed that the amount of Ag was uniform throughout the spike and the core (Figure 8a'-b'), while it was higher at the side wall of the spike for 100 μM $AgNO_3$, which supports our hypothesis that a monolayer of silver stabilizes the surface Au atoms (Figure 8c'-d'). Moreover, silver deposition increased at the core at high $AgNO_3$ concentration (110 μM, Figure 8e'). This growth mechanism also supports the observed patterns in gold nanorod growth, where silver deposits on the side wall of the rod rather than the tips.[23] We further carried out an area scanned analysis of the EDS map to obtain more information about the amount of Ag present on the gold nanostars (Table S1). Area scan results of the spike at 30 μM $AgNO_3$ show 3.28% (A1), 8.84% (A2), and 4.12% (A3) of Ag present at the tip, side wall, and middle portion of the spike, respectively, which reveals that the amount of Ag was almost uniform on the spike. On the other hand, the amount of Ag was significantly lower at the core (A4, 2.46 % Ag). However, we have seen an increase in the amount of Ag at the side wall of the spike of the stars at 100 μM and 110 μM $AgNO_3$ (36.87% for 100 μM (A7) and 33.70% for 110 μM (A15)) compared to the middle portion of the spike (23.61% for 100 μM (A8) and 13.78% for 110 μM (A16)). Interestingly, we have seen that the amount of Ag increased at core when the concentration increased from 100 μM (8.34 % Ag (A10)) to 110 μM (25.05 % Ag (A13)) which supports our hypothesis that the observed LSPR blue shift is also due to Ag deposition at the core (Figure 5i).

The concentration of seeds to be added to the growth solution is also a very important parameter to monitor, as the seed is the primary nucleation center from which the spikes are formed. Moreover, it is reported that multibranched hollow gold nanostars can be formed in the absence of seeds.[10] We have determined the concentration of seeds following a reported method,[44] and investigated their effect by increasing their concentration from 0.02 nM to 0.14 nM, in 0.04 nM increments (Figure 9a-d and Figure S11). We determined that 0.14 nM is the smallest amount of seeds necessary to achieve 6-branched stars with high monodispersity (Figure 9d), which is associated to both spike number and spike length reduction (Figure 9a-d). On the contrary, multibranched stars were formed at 0.02 nM seed concentration (Figure 9a). Interestingly, the spike number never increased above six by increasing the concentration of seeds above 0.1 nM (Figure 9c). The high sample monodispersity achieved for 0.14 nM seeds was evidenced in the UV-Vis spectra reported in Figure 8e in the form of narrower LSPR bands (green curve) compared to what observed at lower seed concentrations. During the growth process, the availability of free gold atoms is very high when the concentration of seeds in the growth solution is low. These gold atoms can easily associate to the seeds and generate nucleation centers in high numbers, thus leading to the formation of multibranched stars. However, the availability of free gold atoms saturates at or above 0.1 nM seed concentration, thus leading to nanostars with fewer spikes and shorter spike lengths, as larger amounts of seeds at equal Au concentration create more primary growth centers. A similar observation was reported by Barbosa et al. who noted that the branching of PVP-capped gold nanostars increased by decreasing seed concentration in the growth solution.[45]

One of the most interesting aspects of this synthesis is the possibility to leverage the interplay between Triton X, ascorbic acid, and seeds to modify the number of branches in the nanostars. For instance, in Figure 1 we have seen that the number of branches can be increased by either decreasing Triton X (Figure 2c, and 2f) or by increasing ascorbic acid (Figure 2g, and 2h) at constant seed concentration. In Figure 9 (9a-d) the number of branches was increased by decreasing the seed amount when the other variables were kept constant. To examine how these three variables are connected to each other, we ran two additional control experiments starting from the multibranched stars reported in Figure 9a and 9b. These nanoparticles were synthesized in conditions ideal to specifically obtain multibranched stars (0.15 M Triton X, 1.6 mM ascorbic acid, 100 μM of $AgNO_3$, and either 0.02 nM or 0.06 nM seeds). In our first control, we increased the concentration of Triton X from 0.15 M to 0.3 M, while the other concentrations were kept constant, and observed that in both cases the morphology changed from multibranched to 6-branched stars (Figure 9f-g). In the second control experiment, we decreased the concentration of ascorbic acid form 1.6 mM to 0.8 mM keeping the other variables constant. In these conditions, we did observe a decrease in the number of branches with decreasing ascorbic acid concentration (Figure 9h-i), but this was not sufficient to produce 6-branched nanostars at 0.02 nM seed concentration (Figure 9h). These results show that the basic process of forming the 6-branched stars can be tweaked by independently modifying the concentration of Triton X, ascorbic acid, and seeds, which provides a useful knob to rationally tune morphology.

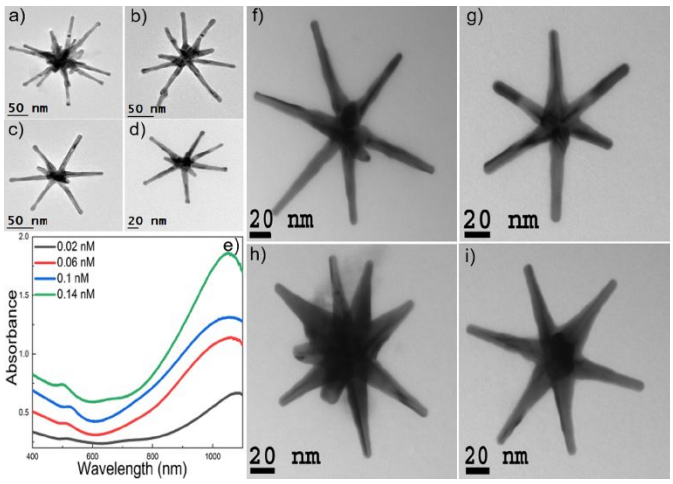

Figure 9. (a-d) TEM micrographs of gold nanostars synthesized by adding different amounts of seeds (0.02 nM (a), 0.06 nM (b), 0.1 nM (c), and 0.14 nM (d)) to the growth solution containing 0.15 M Triton X, 1.6 mM ascorbic acid, and 100 µM of $AgNO_3$. e) UV-Vis spectra (normalized) of the nanostars at different concentration of seeds showing a blue-shifted narrower LSPR band with increasing seed concentration, which indicates that lower branching and higher monodispersity of the stars can be achieved at 0.14 nM seeds concentration. (f-g) TEM micrographs of gold nanostars synthesized by adding different amounts of seeds (0.02 nM (f), and 0.06 nM (g)) to the growth solution containing 0.3 M Triton X, 1.6 M ascorbic acid, and 100 µM of $AgNO_3$. (h-i) TEM micrographs of gold nanostars synthesized by adding a different amount of seeds (0.02 nM (h), and 0.06 nM (i)) to the growth solution containing 0.15 M Triton X, 0.8 mM ascorbic acid, and 100 µM of $AgNO_3$. A decrease in spike number from figures a and b is evident. At low ascorbic acid concentration (h and i) 6-branched nanostars cannot be obtained at low seed concentration, as opposed to the other conditions.

Conclusion

In this study, we have reported a detailed systematic study of the seed-mediated growth mechanism of 6-branched gold nanostars. The interplay of various synthetic parameters (Triton X, ascorbic acid, $AgNO_3$, and seed concentrations) is shown to influence the growth and final morphology of the nanostars. After extrapolating the fundamental growth parameters, and identifying the ideal parameter space for Triton X, ascorbic acid, $AgNO_3$, and seeds to yield to the expected 6-branched products, we explored in detail the role of the nature of the seeds and the concentration of $AgNO_3$. Analysis of the kinetic data and microscopic images reveals that during this synthesis the single crystalline seeds transform into two different types of intermediate seeds- multiply-twinned intermediate seeds for multibranched stars and penta-twinned intermediate seeds for 6-branched stars. Moreover, the evolution of the spikes of 6-branched stars shows that the shape and size of the spikes are highly dependent on $AgNO_3$ concentration, proceeding via a common intermediate having maximum spike length (100 nm), with final spike length determined by the amount of $AgNO_3$ in solution. We have demonstrated the important role of silver in the stabilization of the evolving crystal, confirmed by the observation that at low $AgNO_3$ concentrations kinetically-trapped nanostars, at 5-minute time points, evolve substantially before reaching thermodynamic equilibrium at 12 hours. Most importantly, the presence of metallic silver both at the side walls of the spikes (at low $AgNO_3$ concentration) at also at the core (at high $AgNO_3$ amounts) reveals in detail the importance of this reagent in tuning nanostar morphology: Increasing amounts of deposited silver appear to stabilize the five-fold twinned morphology, which would instead be lost at low Ag concentrations due to the substantial strain present in highly-curved twinned regions. These nanostars display high monodispersity, batch-to-batch reproducibility, and plasmon tunability between the visible and the short-wave infrared, which could prove extremely useful in several quantitative applications or fundamental studies for which the rational design of multibranched nanoparticles is necessary. Looking ahead, it is possible to envision how this synthesis could lend itself as a model for the implementation of machine learning tools in materials design. In particular, the simple nanoparticle morphology characterized by a limited number of branches, the high shape anisotropy, the dependence of the LSPR band position on the tunable morphology of the branches, and the straightforward synthetic conditions, could be leveraged to implement highly parallelized automated syntheses. In turn, the thousands of samples produced could be employed to train and test machine learning algorithms to explore and understand uncharted multidimensional parameter spaces and thus lead to discovering novel nanoparticle morphologies that would otherwise remain untapped.

Experimental section

Materials. Gold (III) chloride trihydrate ($HAuCl_4.3H_2O$), silver nitrate ($AgNO_3$; 99.995%), L(+)-ascorbic acid, sodium borohydride ($NaBH_4$), and TritonX-100 were purchased from Sigma-Aldrich. All these chemicals were used without further purification. Ultrapure MilliQ water (18.2 MΩ.cm) was used in all syntheses. All glassware was aqua regia cleaned before each synthesis.

Instrumentation. Absorption spectra were collected on a Thermo Scientific Evolution 300 UV-Visible spectrophotometer using a quartz cuvette with 1 cm path. Nanoparticle morphology was determined using a Topcon 002B TEM. HRTEM analysis was performed on a JEOL 2010 F high-resolution transmission electron microscope. The particle sizes (spike length, spike width) were analyzed using ImageJ. Particle morphology was analyzed using Gatan DigitalMicrograph (TM) 3.11.1 for GMS 1.6.1. The values of averaged spacing were obtained from Fourier transform analysis of high-magnification images.

Scanning transmission electron microscopy (STEM) was carried out using a FEI Titan Themis transmission electron microscope (TEM) operated at 200kV. Energy dispersive X-ray spectroscopy maps (EDX maps) were obtained in a scanning mode of TEM (STEM). The point resolution in this aberration-corrected mode is 0.08nm. 1nm resolution EDX maps with an average beam current of 100pA are routine with this microscope.

STEM tomography was obtained collecting a tilt series (from -60° to +60° in 10° steps) using a FEI Titan Themis 60-300 operated at 300 kV. Tomographic reconstruction was obtained using a software based on TomToolbox for Matlab[46] Alignment of the tilt series was carried out via TomoJ.[47] Masked SIRT and DART was performed according to Zürner et al.[48] Discrete tomography of demanding samples was based on a modified SIRT algorithm.[48]

Synthesis of 6-branched Gold Nanostars. The synthesis of 6 branched gold nanostars was first proposed by Pallavicini et al.28 However, their nanoparticles did not display sufficient purity and monodispersity. We, therefore, modified and varied the synthetic parameters to achieve high monodispersity and tunable morphology. Briefly, the seed solution was prepared by addition of a freshly prepared ice-cold solution of $NaBH_4$ (0.6 ml, 0.01 M) into a solution mixture of $HAuCl_4$ (10 ml, 0.25 mM) and Triton X, whose concentration was ranging from 0.01 to 0.3 M. The solution turned immediately from pale yellow to orange after addition of $NaBH_4$. The mixture was stirred for 2 minutes and aged for 10 minutes at 4°C before use.

The growth solution was prepared by adding 0.4 ml of 25 mM $HAuCl_4$ solution to a 20 ml Triton-X solution where the concentration of Triton-X was the same for both the seed and growth solutions. This step was followed by addition of ascorbic acid (ranging from 0.8 to 3.9 mM), $AgNO_3$ (ranging from 30 to 110 μM), and Au seeds (ranging from 0.02 nM to 0.14 nM) to the growth solution. The solution was stirred for 12 hours and then centrifuged at 4,000 g for 10 min and dispersed with 5 ml of Ultrapure MilliQ water (18.2 MΩ.cm).

Arrested Growth Studies. We have observed that n-pentanethiol works best to trap reaction intermediates compared to the more commonly used mPEG-SH (MW 5000), as we observed surface modifications and nanoparticle restructuring using the latter. Briefly, an aliquot (1 ml) of growth solution at the desired time was added to the solution of 1 ml 8.4 mM n-pentane in ethanol. Then, the solution was mixed well and centrifuged at 8000 g for 10 minutes. UV-Vis and TEM analysis of the particles were performed immediately after re-dispersion of the particles in 500 μL of MilliQ water.

Conflicts of interest

There are no conflicts to declare.

Author information

Corresponding Author

* lfabris@soe.rutgers.edu

ORCID: 0000-0002-7089-5175

Acknowledgments

This work was funded through National Science Foundation grant CHE-1415881.

References

1. Indrasekara, A. S. D. S.; Meyers, S.; Shubeita, S.; Feldman, L. C.; Gustafsson, T.; Fabris, L., Nanoscale 2014, 6 (15), 8891-8899.

2. Wang, Y.; Serrano, A. B.; Sentosun, K.; Bals, S.; Liz-Marzán, L. M., Small 2015, 11 (34), 4314-4320.

3. Kedia, A.; Kumar, P. S., Journal of Materials Chemistry C 2013, 1 (30), 4540-4549.

4. Khoury, C. G.; Vo-Dinh, T., The journal of physical chemistry. C, Nanomaterials and interfaces 2008, 2008 (112), 18849-18859.

5. Trigari, S.; Rindi, A.; Margheri, G.; Sottini, S.; Dellepiane, G.; Giorgetti, E., Journal of Materials Chemistry 2011, 21 (18), 6531-6540.

6. Hsiangkuo, Y.; Christopher, G. K.; Hanjun, H.; Christy, M. W.; Gerald, A. G.; Tuan, V.-D., Nanotechnology 2012, 23 (7), 075102.

7. Atta, S.; Tsoulos, T. V.; Fabris, L., The Journal of Physical Chemistry C 2016, 120 (37), 20749-20758.

8. Kawamura, G.; Yang, Y.; Fukuda, K.; Nogami, M., Materials Chemistry and Physics 2009, 115 (1), 229-234.

9. Ndokoye, P.; Li, X.; Zhao, Q.; Li, T.; Tade, M. O.; Liu, S., Journal of Colloid and Interface Science 2016, 462, 341-350.

10. Blanch, A. J.; Döblinger, M.; Rodríguez-Fernández, J., Small 2015, 11 (35), 4550-4559.

11. Niu, W.; Chua, Y. A. A.; Zhang, W.; Huang, H.; Lu, X., Journal of the American Chemical Society 2015, 137 (33), 10460-10463.

12. Ramsey, J. D.; Zhou, L.; Kyle Almlie, C.; Lange, J. D.; Burrows, S. M., New Journal of Chemistry 2015, 39 (12), 9098-9108.

13. Guerrero-Martínez, A.; Barbosa, S.; Pastoriza-Santos, I.; Liz-Marzán, L. M., Current Opinion in Colloid & Interface Science 2011, 16 (2), 118-127.

14. Sajitha, M.; Vindhyasarumi, A.; Gopi, A.; Yoosaf, K., RSC Advances 2015, 5 (119), 98318-98324.

15. Ahmad, N.; Wang, G.; Nelayah, J.; Ricolleau, C.; Alloyeau, D., Nano Letters 2017, 17 (7), 4194-4201.

16. Pu, Y.; Zhao, Y.; Zheng, P.; Li, M., Inorganic Chemistry 2018, 57 (14), 8599-8607.

17. Yuan, H.; Ma, W.; Chen, C.; Zhao, J.; Liu, J.; Zhu, H.; Gao, X., Chemistry of Materials 2007, 19 (7), 1592-1600.

18. Tong, W.; Katz-Boon, H.; Walsh, M. J.; Weyland, M.; Etheridge, J.; Funston, A. M., Chemical Communications 2018, 54 (24), 3022-3025.

19. Tong, W.; Walsh, M. J.; Mulvaney, P.; Etheridge, J.; Funston, A. M., The Journal of Physical Chemistry C 2017, 121 (6), 3549-3559.

20. Nikoobakht, B.; El-Sayed, M. A., Chemistry of Materials 2003, 15 (10), 1957-1962.

21. Hubert, F.; Testard, F.; Spalla, O., Langmuir 2008, 24 (17), 9219-9222.

22. Liu, M.; Guyot-Sionnest, P., The Journal of Physical Chemistry B 2005, 109 (47), 22192-22200.

23. Orendorff, C. J.; Murphy, C. J., The Journal of Physical Chemistry B 2006, 110 (9), 3990-3994.

24. Jackson, S. R.; McBride, J. R.; Rosenthal, S. J.; Wright, D. W., Journal of the American Chemical Society 2014, 136 (14), 5261-5263.

25. Sau, T. K.; Murphy, C. J., Langmuir 2004, 20 (15), 6414-6420.

26. Xie, J.; Lee, J. Y.; Wang, D. I. C., Chemistry of Materials 2007, 19 (11), 2823-2830.

27. Bakr, O. M.; Wunsch, B. H.; Stellacci, F., Chemistry of Materials 2006, 18 (14), 3297-3301.

28. Jeong, G. H.; Lee, Y. W.; Kim, M.; Han, S. W., Journal of Colloid and Interface Science 2009, 329 (1), 97-102.

29. Senthil Kumar, P.; Pastoriza-Santos, I.; Rodriguez-Gonzalez, B.; Garcia de Abajo, J.; Liz-Marzan, L., Nanotechnology 2008, 19 (1), 015606.

30. Tsoulos, T. V.; Atta, S.; Lagos, M. J.; Batson, P. E.; Tsilomelekis, G.; Fabris, L. ChemRxiv. 2018, DOI: 10.26434/ chemrxiv.6552743.

31. Pallavicini, P.; Dona', A.; Casu, A.; Chirico, G.; Collini, M.; Dacarro, G.; Falqui, A.; Milanese, C.; Sironi, L.; Taglietti, A., Chemical Communications 2013, 49 (56), 6265-6267.

32. Mandal, A. B.; Nair, B. U.; Ramaswamy, D., Langmuir 1988, 4 (3), 736-739.

33. Takenaka, Y.; Kawabata, Y.; Kitahata, H.; Yoshida, M.; Matsuzawa, Y.; Ohzono, T., Journal of Colloid and Interface Science 2013, 407, 265-272.

34. Zhou, H.; Jia, H.; Zhang, A.; Zhang, L.; Jia, C.; Zheng, L., Journal of Molecular Liquids 2015, 208, 27-33.

35. Ahmed, W; Kooij, E. S.; van Silfhout, A.; Poelsema, B., Nanotechnology 2010, 21 (12), 125605.

36. Novo, C.; Mulvaney, P., Nano Letters 2007, 7 (2), 520-524.

37. Kuo, C.-H.; Huang, M. H., Langmuir 2005, 21 (5), 2012-2016.

38. Sau, T. K.; Rogach, A. L.; Döblinger, M.; Feldmann, J., Small 2011, 7 (15), 2188-2194.

39. Fales, A. M.; Yuan, H.; Vo-Dinh, T., The Journal of Physical Chemistry C 2014, 118 (7), 3708-3715.

40. Keul, H. A.; Möller, M.; Bockstaller, M. R., Langmuir 2007, 23 (20), 10307-10315.

41. Alpay, D.; Peng, L.; Marks, L. D., The Journal of Physical Chemistry C 2015, 119 (36), 21018-21023.

42. Langille, M. R.; Personick, M. L.; Zhang, J.; Mirkin, C. A., Journal of the American Chemical Society 2012, 134 (35), 14542-14554.

43. Personick, M. L.; Langille, M. R.; Zhang, J.; Mirkin, C. A., Nano Letters 2011, 11 (8), 3394-3398.

44. Liu, X.; Atwater, M.; Wang, J.; Huo, Q., Colloids and Surfaces B: Biointerfaces 2007, 58 (1), 3-7.

45. Barbosa, S.; Agrawal, A.; Rodríguez-Lorenzo, L.; Pastoriza-Santos, I.; Alvarez-Puebla, R. A.; Kornowski, A.; Weller, H.; Liz-Marzán, L. M., Langmuir 2010, 26 (18), 14943-14950.

46. Nickell, S.; Förster, F.; Linaroudis, A.; Net, W.; Beck, F.; Baumeister, W.; Plitzko, J., Journal of Structural Biology 2005, 149 (3), 227–234.

47. Messaoudil, C.; Boudier, T.; Sorzano, C.; Marco, S., BMC bioinformatics 2007, 8(1), 288.

48. Zürner, A.; Döblinger, M.; Cauda, V.; Wei, R.; Bein, T., Ultramicroscopy 2012, 115, 41-49.